1   **Developing a monthly radiative kernel for surface albedo change from satellite**

2   **climatologies of Earth's shortwave radiation budget: CACK v1.0**

4   Ryan M. Bright[1*] and Thomas L. O'Halloran[2,3]

6   1 – Norwegian Institute of Bioeconomy Research, Ås, Norway

7   2 – Department of Forestry and Environmental Conservation, Clemson University, Clemson,

8   South Carolina, USA.

9   3 – Baruch Institute of Coastal Ecology and Forest Science, Clemson University,

10   Georgetown, South Carolina, USA

11   [*]Contact: ryan.bright@nibio.no

13   **Abstract**

14   Due to the potential for land use / land cover change (LULCC) to alter surface albedo, there is

15   need within the LULCC science community for simple and transparent tools for predicting

16   radiative forcings (ΔF) from surface albedo changes ($\Delta \alpha_s$). To that end, the radiative kernel

17   technique – developed by the climate modeling community to diagnose internal feedbacks

18   within general circulation models (GCMs) – has been adopted by the LULCC science

19   community as a tool to perform offline ΔF calculations for $\Delta \alpha_s$. However, the codes and

20   data behind the GCM kernels are not readily transparent, and the climatologies of the

21   atmospheric state variables used to derive them vary widely both in time period and duration.

22   Observation-based kernels offer an attractive alternative to GCM-based kernels and could be

23   updated annually at relatively low costs. Here, we present a radiative kernel for surface

24   albedo change founded on a novel, simplified parameterization of shortwave radiative transfer

25   driven with inputs from the Clouds and the Earth's Radiant Energy System (CERES) Energy

26   Balance and Filled (EBAF) products. When constructed on a 16-year climatology (2001-

27   2016), we find that the CERES-based albedo change kernel – or CACK – agrees remarkably

28   well with the mean kernel of four GCMs (rRMSE = 14%). When the novel parameterization

29   underlying CACK is applied to emulate two of the GCM kernels using their own boundary

30   fluxes as input, we find even greater agreement (mean rRMSE = 7.4%), suggesting that this

31   simple and transparent parameterization represents a credible candidate for a satellite-based

32   alternative to GCM kernels. We document and compute the various sources of uncertainty

33   underlying CACK and include them as part of a more extensive dataset (CACK v1.0) while

34   providing examples showcasing its application.

35   **Keywords:** GCM, radiative forcing, land use change, land cover change, LULCC

37   **1. Introduction**

38   Diagnosing changes to the shortwave radiation balance at the top-of-the-atmosphere (TOA)

39   resulting from changes to albedo at the surface ($\Delta\alpha_s$) is an important step in predicting

40   climate change. However, outside the climate science community, many researchers do not

41   have the tools to convert $\Delta\alpha$ to the climate-relevant ΔF measure (Bright, 2015; Jones et al.,

42   2015), which requires a detailed representation of the atmospheric constituents that absorb or

43   scatter solar radiation (e.g. cloud, aerosols, and gases) and a sophisticated radiative transfer

44   code. For single points in space or for small regions, these calculations are typically

45   performed offline – meaning without feedbacks to the atmosphere (e.g., (Randerson et al.,

46   2006))). Large-scale investigations (e.g. Amazonian or pan-boreal LULCC (Bonan et al.,

47   1992; Dickinson and Henderson-Sellers, 1988)) typically prescribe the land surface layer in a

48   GCM with initial and perturbed states, allowing the radiative transfer code to interact with the

49   rest of the model. While this has the benefit of allowing interaction and feedbacks between

50   surface albedo and scattering or absorbing components of the model, such an approach is

computationally expensive and thereby restricts the number of LULCC scenarios that can be

investigated (Atwood et al., 2016). Consequently, this method does not meet the needs of

some modern LULCC studies which may require millions of individual land cover transitions

to be evaluated cost effectively (Ghimire et al., 2014; Lutz and Howarth, 2015).

Within the LULCC science community, two methods have primarily met the need for

efficient ΔF calculations from $\Delta \alpha_s$: simplified parameterizations of atmospheric transfer of

shortwave radiation (Bozzi et al., 2015; Bright and Kvalevåg, 2013; Caiazzo et al., 2014;

Carrer et al., 2018; Cherubini et al., 2012; Muñoz et al., 2010), and radiative kernels (Ghimire

et al., 2014; O'Halloran et al., 2012; Vanderhoof et al., 2013) derived from sophisticated

radiative transfer schemes embedded in GCMs (Block and Mauritsen, 2014; Pendergrass et

al., 2018; Shell et al., 2008; Soden et al., 2008). Simplified parameterizations of the LULCC

science community have not been evaluated comprehensively in space and time. Bright &

Kvalevåg (2013) evaluated the shortwave ΔF parameterization of Cherubini *et al.* (2012)

when applied at several globally distributed sites on land, finding inconsistencies in

performance at individual sites despite good overall cross-site performance. Radiative kernels

(Block and Mauritsen, 2014; Pendergrass et al., 2018; Shell et al., 2008; Soden et al., 2008) –

while being based on state-of-the-art models of radiative transfer – have the downside of

being model-dependent and not readily transparent. While the radiative transfer codes behind

them are well-documented, the scattering components (i.e. aerosols, gases, and clouds)

affecting transmission have many simplifying parameterizations, vary widely across models,

and may contain significant biases (Dolinar et al., 2015; Wang and Su, 2013). An additional

downside is that the atmospheric state climatologies used to compute the GCM kernels vary

widely in their time periods (i.e., from pre-industrial to the year 2007) and durations (from 1

to 1,000 yrs). The application of a state-dependent GCM kernel that is outdated may be

undesirable in regions undergoing rapid changes in cloud cover or aerosol optical depth, such

as in the northwest United States (Free and Sun, 2014) and in southern and eastern Asia

(Srivastava, 2017; Zhao et al., 2018), respectively. An albedo change kernel based on Earth-

orbiting satellite products could be updated annually to capture changes in atmospheric state

at relatively low costs.

The NASA Clouds and the Earth's Radiant Energy System (CERES) Energy Balance and

Filled (EBAF) products (CERES Science Team, 2018a, b), which are based largely on

satellite optical remote sensing, provide the monthly mean boundary fluxes and other

atmospheric state information (e.g., cloud area fraction, cloud optical depth) that could be

used to develop a more empirically-based alternative to the GCM-based kernels. The latest

EBAF-TOA Ed4.0 (version 4.0) products have many improvements with respect to the

previous version (version 2.8, Loeb et al. 2009), including the use of advanced and more

consistent input data, retrieval of cloud properties, and instrument calibration (Kato et al.,

2018; Loeb et al., 2017).

Here, we present an albedo change kernel based on the CERES EBAF v4 products – or

CACK. Underlying CACK is a simplified model of shortwave radiative transfer through a

one-layer atmosphere. The model form (or parameterization) is selected after a two-stage

performance evaluation of six model candidates: two analytical, one semi-empirical, and

three empirical. An initial performance screening is implemented where all six model

candidates are driven with a 16-year climatology (January 2001 – December 2016) of

monthly all-sky boundary fluxes from CERES, with the resulting kernels benchmarked both

qualitatively and quantitatively against the mean of four GCM-based kernels (Block and

Mauritsen, 2014; Pendergrass et al., 2018; Shell et al., 2008; Soden et al., 2008). Top model

candidates from the initial performance screening are then subjected to an additional

performance evaluation where they are applied to emulate two GCM kernels using their own

100   boundary fluxes as input, which eliminates possible biases related to differences in the GCM

101   representation of clouds or other atmosphere state variables.

102   We start in Section 2 by providing a brief overview of existing approaches applied in LULCC

103   climate studies for estimating ΔF from $\Delta \alpha$. We then present the six model candidates in

104   Section 3. Section 4 describes the model evaluation and uncertainty quantification methods,

105   in addition to two application examples. Results are presented in Section 5, while Section 6

106   discusses the merits and uncertainties of a CERES-based kernel relative to GCM-based

107   kernels.

108   **2 Review of existing approaches**

109   Earth's energy balance (at TOA) in an equilibrium state can be written:

110    $$0 = F = LW_\uparrow^{TOA} - (SW_\downarrow^{TOA} - SW_\uparrow^{TOA}) \tag{1}$$

111   where the equilibrium flux F is a balance between the net solar energy inputs ($SW_\downarrow^{TOA} - SW_\uparrow^{TOA}$

112   ) and thermal energy output ($LW_\uparrow^{TOA}$). Perturbing this balance results in a radiative forcing

113   ΔF, while perturbing the shortwave component is referred to as a shortwave radiative forcing

114   and may be written as:

115    $$\Delta F = \Delta(SW_\downarrow^{TOA} - SW_\uparrow^{TOA}) = \Delta SW_\downarrow^{TOA}\left(1 - \frac{SW_\uparrow^{TOA}}{SW_\downarrow^{TOA}}\right) - SW_\downarrow^{TOA}\left(\Delta\frac{SW_\uparrow^{TOA}}{SW_\downarrow^{TOA}}\right) \tag{2}$$

116   where the shortwave radiative forcing results either from changes to solar energy inputs (

117    $\Delta SW_\downarrow^{TOA}$) or from internal perturbations within the Earth system ($\Delta\frac{SW_\uparrow^{TOA}}{SW_\downarrow^{TOA}}$). The latter can

118   be brought about by changes to the reflective properties of Earth's surface which is the focus

119   of this paper.

a. GCM-based radiative kernels

The radiative kernel technique was developed as a way to assess various climate feedbacks from climate change simulations across multiple climate models in a computationally efficient manner (Shell et al., 2008; Soden et al., 2008). A radiative kernel is defined as the differential response of an outgoing radiation flux at TOA to an incremental change in some climate state variable -- such as water vapor, air temperature, or surface albedo (Soden et al., 2008). To generate a radiative kernel for a change in surface albedo with a GCM, the prescribed surface albedo change is perturbed incrementally by 1%, and the response by the outgoing shortwave radiation flux at TOA is recorded:

$$\Delta SW_\uparrow^{TOA} = SW_\uparrow^{TOA}(\alpha_s + \Delta\alpha_s) - SW_\uparrow^{TOA}(\alpha_s) = \frac{\partial SW_\uparrow^{TOA}}{\partial \alpha_s}\Delta\alpha_s \equiv K_{\alpha_s}\Delta\alpha_s \tag{3}$$

where $SW_\uparrow^{TOA}$ is the outgoing shortwave flux at TOA and K_{α_s} is the radiative kernel (in Wm^{-2}) which can then be used with Eq. (1) to estimate an instantaneous shortwave radiative forcing (ΔF) at TOA:

$$F + \Delta F = LW_\uparrow^{TOA} - (SW_\downarrow^{TOA} - SW_\uparrow^{TOA} + K_{\alpha_s}\Delta\alpha_s)$$
$$\Delta F = -K_{\alpha_s}\Delta\alpha_s \tag{4}$$

To the best of our knowledge, four albedo change kernels have been developed based on the following GCMs: the Community Atmosphere Model version 3, or CAM3 (Shell et al., 2008), the Community Atmosphere Model version 5, or CAM5 (Pendergrass et al., 2018), the European Center and Hamburg model version 6, or ECHAM6 (Block and Mauritsen, 2014), and the Geophysical Fluid Dynamics Laboratory model version AM2p12b, or GFDL (Soden et al., 2008). These four GCM kernels vary in their vertical and horizontal resolutions, their parameterizations of shortwave radiative transfer, and their prescribed atmospheric state climatologies. These differences are summarized in Table 1. Apart from differences in their

142 prescribed atmospheric background states and radiative transfer schemes, a major source of

143 uncertainty in GCM-based kernels is related to the GCM representation of atmospheric liquid

144 water/ice associated with convective clouds; of the four aforementioned GCMs, only CAM5

145 and GFDL attempt to model the effects of convective core ice and liquid in their radiation

146 calculations (Li et al., 2013).

147

148 < Table 1 >

149

150 *b. Single-layer atmosphere models of shortwave radiation transfer*

151 Within the atmospheric science community, various simplified analytical or semi-empirical

152 modeling frameworks have been developed, either to diagnose effective surface and

153 atmospheric optical properties from climate model outputs, or to study the relative

154 contributions of changes to these properties on shortwave flux changes at the top and bottom

155 of the atmosphere (Atwood et al., 2016; Donohoe and Battisti, 2011; Kashimura et al., 2017;

156 Qu and Hall, 2006; Rasool and Schneider, 1971; Taylor et al., 2007; Winton, 2005; Winton,

157 2006). While these frameworks all treat the atmosphere as a single layer, they differ by

158 whether or not the reflection and transmission properties of this layer are assumed to have a

159 directional dependency (Stephens et al., 2015) and by whether or not inputs other than those

160 derived from the boundary fluxes are required (e.g. cloud properties; (Qu and Hall, 2006)).

161 Winton (2005) presented a semi-empirical four-parameter optical model to account for the

162 directional dependency of up- and downwelling shortwave fluxes through the one-layer

163 atmosphere and found good agreement (rRMSE < 2% globally) when benchmarked to online

164 radiative transfer calculations. Also considering a directional dependency of the atmospheric

165 optical properties, Taylor et al. (2007) presented a two-parameter analytical model where

166 atmospheric absorption was assumed to occur at a level above atmospheric reflection. The

167 analytical model of Donohoe and Battisti (2011) subsequently relaxed the directional

168 dependency assumption and found the atmospheric attenuation of the surface albedo

169 contribution to planetary albedo to be 8% higher than the model of Taylor et al. (2007).

170 Elsewhere, Qu & Hall (2006) developed an analytical framework making use of additional

171 atmospheric properties such as cloud cover fraction, cloud optical thickness, and the clear-sky

172 planetary albedo, which proved highly accurate when model estimates of planetary albedo

173 were evaluated against climate models and satellite-based datasets.

174 *c. Simple empirical parameterizations of the LULCC science community*

175 Two simple empirical parameterizations of shortwave radiative transfer have been widely

176 applied within the LULCC science community for estimating ΔF from $\Delta \alpha_s$ (Bozzi et al.,

177 2015; Caiazzo et al., 2014; Carrer et al., 2018; Cherubini et al., 2012; Lutz et al., 2015;

178 Muñoz et al., 2010). While these parameterizations are also based on a single-layer

179 atmosphere model of shortwave radiative transfer, at the core of these parameterizations is the

180 fundamental assumption that radiative transfer is wholly independent of (or unaffected by)

181 $\Delta \alpha_s$. In other words, they neglect the change in the attenuating effect of multiple reflections

182 between the surface and the atmosphere that accompanies a change to the surface albedo.

183 Nevertheless, due to their simplicity and ease of application they continue to be widely

184 employed in climate research.

185 **3. Kernel model candidates**

186 The six candidate models (or parameterizations) for a CERES-based albedo change kernel

187 (CACK) are presented henceforth. All requisite variables and their derivatives may be

188 obtained directly from the CERES EBAF v4 products (at monthly and $1° \times 1°$ resolution) and

189 are presented in Table 2. To improve readability, temporal and spatial indexing is neglected

190 and all terms presented henceforth in Section 3 denote the monthly pixel means.

191 < Table 2 >

192 *a. Analytical kernels*

193 The first kernel candidate may be analytically-derived from the CERES EBAF all-sky

194 boundary fluxes and their derivatives. The surface contribution to the outgoing shortwave

195 flux at TOA $SW_{\uparrow,SFC}^{TOA}$ can be expressed (Donohoe and Battisti, 2011; Stephens et al., 2015;

196 Winton, 2005) as:

197 $$SW_{\uparrow,SFC}^{TOA} = SW_{\downarrow}^{TOA} \alpha_s \frac{(1-r-a)^2}{(1-r\alpha_s)} \tag{5}$$

198 where r is a single pass atmospheric reflection coefficient, a is a single pass atmospheric

199 absorption coefficient, $SW_{\downarrow}^{TOA}$ is the extraterrestrial (downwelling) shortwave flux at TOA,

200 and α_s is the surface albedo (defined in Table 2). The expression in the denominator of the

201 righthand term represents a fraction attenuated by multiple reflections between the surface

202 and the atmosphere. This model assumes that the atmospheric optical properties r and a are

203 insensitive to the origin and direction of shortwave fluxes – or in other words – that they are

204 isotropic.

205 The single-pass reflectance coefficient is calculated from the system boundary fluxes (Table

206 2) following Winton (2005) and Kashimura *et al.* (2017):

207 $$r = \frac{SW_{\downarrow}^{TOA} SW_{\uparrow}^{TOA} - SW_{\downarrow}^{SFC} SW_{\uparrow}^{SFC}}{SW_{\downarrow}^{TOA\ 2} - SW_{\uparrow}^{SFC\ 2}} \tag{6}$$

208 while the single-pass absorption coefficient a is given as:

209 $$a = 1 - r - T(1 - \alpha_s r) \tag{7}$$

210 where T is the clearness index (defined in Table 2). Our interest is in quantifying the $SW_{\uparrow,SFC}^{TOA}$

211 response to an albedo perturbation at the surface – or the partial derivative of $SW_{\uparrow,SFC}^{TOA}$ with

212 respect to α in Eq. (5):

$$213 \quad \frac{\partial SW_{\uparrow}^{TOA}}{\partial \alpha_s} \Delta \alpha_s = K_{\alpha_s}^{ISO} \Delta \alpha_s = \frac{SW_{\downarrow}^{TOA}(1-r-a)^2}{(1-r\alpha_s)^2} \Delta \alpha_s \quad\quad (8)$$

214 where $K_{\alpha_s}^{ISO}$ is referred to henceforth as the *Isotropic* kernel.

215 The second analytical kernel is based on the model of Qu and Hall (2006) which makes use of

216 auxiliary cloud property information commonly provided in satellite-based products of

217 Earth's radiation budget – including CERES EBAF – such as cloud cover area fraction, cloud

218 visible optical depth, and clear-sky planetary albedo. This model links all-sky and clear-sky

219 effective atmospheric transmissivities of the earth system through a linear coefficient k

220 relating the logarithm of cloud visible optical depth to the effective all-sky atmospheric

221 transmissivity:

$$222 \quad k = \frac{(T_{a,CLR})-(T_a)}{\ln(\tau+1)} \quad\quad (9)$$

223 where $T_{a,CLR}$ is the clear-sky effective system transmissivity, T_a is the all-sky effective system

224 transmissivity, and τ is the cloud visible optical depth. This linear coefficient can then be

225 used together with the cloud cover area fraction to derive a shortwave kernel based on the

226 model of Qu and Hall (2006) – or $K_{\alpha_s}^{QH06}$:

$$227 \quad \frac{\partial SW_{\uparrow}^{TOA}}{\partial \alpha_s} \Delta \alpha_s = K_{\alpha_s}^{QH06} \Delta \alpha_s = SW_{\downarrow}^{SFC}\left[(T_a)-kc\ln(\tau+1)\right]\Delta \alpha_s \quad\quad (10)$$

228 where c is the cloud cover area fraction.

229 *b. Semi-empirical kernel*

230   The third kernel makes use of three directionally-dependent (anisotropic) bulk optical

231   properties $r_\uparrow$, $t_\uparrow$, and $t_\downarrow$, where the first is the atmospheric reflectivity to upwelling

232   shortwave radiation and the latter two are the atmospheric transmission coefficients for

233   upwelling and downwelling shortwave radiation, respectively (Winton, 2005). It is not

234   possible to derive $r_\uparrow$ analytically from the all-sky boundary fluxes; however, Winton (2005)

235   provides an empirical formula relating upwelling reflectivity $r_\uparrow$ to the ratio of all-sky to clear-

236   sky fluxes incident at surface:

237    $$r_\uparrow = 0.05 + 0.85\left(1 - \frac{SW_\downarrow^{SFC}}{SW_{\downarrow,CLR}^{SFC}}\right) \tag{11}$$

238   where $SW_{\downarrow,CLR}^{SFC}$ is the clear-sky shortwave flux incident at the surface.

239   Knowing $r_\uparrow$, we can then solve for the two remaining optical parameters needed to obtain our

240   kernel:

241    $$t_\downarrow = \frac{SW_\downarrow^{SFC} - r_\uparrow SW_\uparrow^{SFC}}{SW_\downarrow^{TOA}} \tag{12}$$

242    $$t_\uparrow = T_a - \left[t_\downarrow - t_\downarrow(1 - r_\uparrow \alpha_s)\right] \tag{13}$$

243   where T_a is the effective atmospheric transmittance (Table 2) of the earth system.

244   The kernel may now be expressed as:

245    $$\frac{\partial SW_\uparrow^{TOA}}{\partial \alpha_s}\Delta\alpha_s = K_{\alpha_s}^{ANISO}\Delta\alpha_s = \frac{SW_\downarrow^{TOA} t_\downarrow t_\uparrow}{(1 - r_\uparrow \alpha_s)^2}\Delta\alpha_s \tag{14}$$

246   where $K_{\alpha_s}^{ANISO}$ is henceforth referred to as the *Anisotropic* kernel.

247   *c. Existing empirical parameterizations*

248 Although not referred to as "kernels" in the literature *per se*, we present the simple empirical

249 parameterizations as such to ensure consistency with previously described notation and

250 terminology.

251

252 The first candidate parameterization, originally presented in Muñoz *et al*. (2010), makes use

253 of a local two-way transmittance factor based on the local clearness index:

$$\frac{\partial SW_\uparrow^{TOA}}{\partial \alpha_s}\Delta\alpha_s \equiv K_{\alpha_s}^{M10}\Delta\alpha_s = SW_\downarrow^{TOA}T^2\Delta\alpha_s \qquad (15)$$

255 where $SW_\downarrow^{TOA}$ is the local incoming solar flux at TOA, T is the local clearness index, and

256 $\partial SW_\uparrow^{TOA}/\partial\alpha_s$ is the approximated change in the upwelling shortwave flux at TOA due to a

257 change in the surface albedo.

258 The second candidate parameterization, originally proposed in Cherubini *et al*. (2012), makes

259 direct use of the solar flux incident at the surface $SW_\downarrow^{SFC}$ combined with a one-way

260 transmission constant *k*:

$$\frac{\partial SW_\uparrow^{TOA}}{\partial \alpha_s}\Delta\alpha_s \equiv K_{\alpha_s}^{C12}\Delta\alpha_s = SW_\downarrow^{SFC}k\Delta\alpha_s \qquad (16)$$

262 where *k* is based on the global annual mean share of surface reflected shortwave radiation

263 exiting a clear-sky (Lacis and Hansen, 1974; Lenton and Vaughan, 2009) and is hence

264 temporally and spatially invariant. This value – or 0.85 -- is similar to the global mean ratio

265 of forward-to-total shortwave scattering reported in Iqbal (1983). Bright & Kvalevåg (2013)

266 evaluated Eq. (16) at several global locations and found large biases for some regions and

267 months, despite good overall performance globally (rRMSE = 7%; *n* = 120 months).

268 *d. Proposed empirical parameterization*

269   To determine whether the GCM-based kernels could be approximated with sufficient fidelity

270   using other simpler model formulations based on their own boundary data, we applied

271   machine learning to identify potential model forms using GCM shortwave boundary fluxes as

272   input. For the two GCMs kernels in which the GCM's own shortwave boundary fluxes are

273   also made available (CAM5 and ECHAM6), we used machine learning to minimize the sum

274   of squared residuals between the four shortwave boundary fluxes (i.e., $SW_\downarrow^{SFC}$, $SW_\downarrow^{TOA}$,

275     $SW_\uparrow^{SFC}$, $SW_\uparrow^{TOA}$) and the GCM kernel at the monthly time step. The reference dataset

276   consisted of a random global sample of 200,000 monthly kernel grid cells at native model

277   resolution (97% and 32% of all cells for ECHAM6 and CAM5, respectively) of which 50%

278   were used for training and 50% for validation. Models were identified using a form of genetic

279   programming known as symbolic regression (Eureqa®; Nutonian Inc.; (Schmidt and Lipson,

280   2009, 2010)) which searches a wide space of model structures as constrained by user input.

281   In our case, we allowed the model to include the operators (i.e., addition, subtraction,

282   multiplication, division, sine, cosine, tangent, exponential, natural logarithm, factorial, power,

283   square root), but numerical coefficients were forbidden. The model search was allowed to

284   continue until the percent convergence and maturity metrics exceeded 98% and 50%,

285   respectively, at which point more than 1×10^{11} formulae had been evaluated. A parsimonious

286   solution was chosen by minimizing the error metric and model complexity using the Pareto

287   front (Figure S1 of Supporting Information) (Smits and Kotanchek, 2005). Between CAM5

288   and ECHAM6, four common model solutions were found (Table S1 of Supporting

289   Information). The best of these common solutions is subsequently referred to as $K_{\alpha_s}^{BO18}$ and is

290   given as:

291     $$\frac{\partial SW_\uparrow^{TOA}}{\partial \alpha_s}\Delta\alpha_s = K_{\alpha_s}^{BO18}\Delta\alpha_s = SW_\downarrow^{SFC}\sqrt{T}\Delta\alpha_s \qquad (17)$$

4. Kernel model evaluation

a. Initial candidate screening

The four GCM kernels presented in Section 2.a are employed as benchmarks to initially screen the six simple model candidates introduced from Section 3b to 3d. We compute a skill metric analogous to the "relative error" metric used to evaluate GCMs by Anav et al. (2013) that takes into account error in the spatial pattern between a model and an observation. Because we have no true observational reference, our evaluation instead focuses on the disagreement or deviation between CERES and GCM kernels at the monthly time step. Given interannual climate variability in the earth system, the challenge of comparing the multi-year CERES kernel to a single-year GCM kernel can be partially overcome by averaging the four GCM kernels.

Using the multi-GCM mean as the reference, we first compute the absolute deviation $AD_{m,p}^X$ as:

$$AD_{m,p}^X = \left| CERES_{m,p}^X - \overline{GCM}_{m,p} \right| \tag{18}$$

where $CERES_{m,p}^X$ is the kernel for CERES model candidate x in month m and pixel p and $\overline{GCM}_{m,p}$ is the multi-GCM mean of the same pixel and month. $AD_{m,p}^X$ is then normalized to the maximum absolute deviation of all six CERES kernels for the same pixel and month to obtain a normalized absolute deviation, $NAD_{m,p}^X$, which is analogous to the "relative error" metric of Anav et al. (2013) having values ranging between 0 and 1:

$$NAD_{m,p}^X = 1 - \frac{AD_{m,p}^X}{\max(AD_{m,p})} \tag{19}$$

314 where $\max(AD_{m,p})$ is the maximum absolute deviation of all six CERES kernels at pixel p

315 and month m.

316 CERES kernel ranking is based on the mean relative absolute deviation in both space and time

317 – or NAD^X :

318 $$NAD^X = \frac{1}{M}\sum_{m=1}^{M}\frac{1}{P}\sum_{p=1}^{P}NAD_{m,p}^X \tag{20}$$

319 where M is the total number of months (i.e., 12) and P is the total number of grid cells.

320

321 *b. GCM kernel emulation*

322 In order to eliminate any bias related to differences in the atmospheric state embedded in the

323 GCM kernel input climatologies, we emulate them by applying the top candidate models (as

324 identified from the initial performance screening described in section 4a) using the original

325 GCM boundary fluxes as input. Emulation is only done for two of GCM-based kernels since

326 only two of them have provided the accompanying boundary fluxes needed to do so:

327 ECHAM6 (Block and Mauritsen, 2014) and CAM5 (Pendergrass et al., 2018). Emulation

328 enables a more critical evaluation of the functional form of the candidate models in relation to

329 the more sophisticated radiative transfer schemes employed by ECHAM6 (Stevens et al.,

330 2013) and CAM5 (Hurrell et al., 2013).

331 *c. CACK model uncertainty*

332 Following emulation, monthly GCM kernels are then regressed on the monthly kernels

333 emulated with the leading model candidates. The model that best emulates both GCM kernels

334 – as measured in terms of the mean coefficient of determination (R^2) and mean RMSE – is

335 chosen to represent CACK.

336 Three sources of uncertainty are considered for CACK when based on the CERES boundary

337 flux climatology (i.e., 2001-2016 monthly means): 1) *physical variability* 2) *data uncertainty*;

338 and 3) *model error* (Mahadevan and Sarkar, 2009). The first is related to the interannual

339 variability of Earth's atmospheric state and boundary radiative fluxes. The second is related

340 to the uncertainty of the CERES EBAF v4 variables used as input to CACK (including

341 measurement error). The third source of uncertainty is the error related to CACK's model

342 form. CACK's combined uncertainty for any given pixel and month is estimated as follows,

343 where if CACK or y is some non-linear function of the CERES boundary inputs x_1 and x_2

344 that co-vary in time and space, then the combined uncertainty of y – or $\sigma(y)$ – may be

345 expressed as the sum of the *model error* plus the combined *physical variability* and *data*

346 *uncertainty* associated with x_1 and x_2 summed in quadrature (Breipohl, 1970; Clifford, 1973;

347 Green et al., 2017):

$$\sigma(y) \approx \sigma_{ME}(y) + \sqrt{\left(\frac{\partial y}{\partial x_1}\right)^2 \left[\sigma_{PV}(x_1) + \sigma_{DU}(x_1)\right]^2 + \left(\frac{\partial y}{\partial x_2}\right)^2 \left[\sigma_{PV}(x_2) + \sigma_{DU}(x_2)\right]^2 + \sqrt{\left(2\frac{\partial y}{\partial x_1}\frac{\partial y}{\partial x_2}\sigma(x_1,x_2)\right)^2}} \quad (21)$$

349 where $\sigma_{PV}(x_1)$ and $\sigma_{PV}(x_2)$ are the standard deviations of the 16-yr. climatological record of

350 CERES input variables x_1 and x_2, respectively, for a given grid cell and month, $\sigma_{DU}(x_1)$ and

351 $\sigma_{DU}(x_2)$ are the absolute uncertainties of CERES input variables x_1 and x_2, respectively, for

352 a given grid cell and month, $\sigma(x_1,x_2)$ is the covariance within the 16-yr. climatological

353 record between CERES input variables x_1 and x_2 for a given month and grid cell, and σ_{ME} is

354 the monthly grid cell model error. Model error ($\sigma_{ME}(y)$) and data uncertainties ($\sigma_{DU}(x_n)$) for

355 any given grid cell and month are based on the relative RMSE (Supporting Information) and

356 relative uncertainties of CERES boundary terms reported in Kato *et al.* (2018) (cf. Table 8,

357 "Monthly gridded, Ocean + Land") and Loeb *et al.* (2017) (cf. Table 8, "All-sky, *Terra-Aqua*

358   period"). For the model error, we take the mean relative RMSE of the machine learning

359   model solutions for ECHAM5 and CAM5. For the relative uncertainty of the incoming solar

360   flux at TOA ($SW_\downarrow^{TOA}$), we use the 1% "calibration uncertainty" reported in Loeb *et al.* (2017).

361   If CACK's intended application is to estimate a temporally-explicit *ΔF* within the CERES era

362   (i.e., if temporally-explicit rather than the climatological mean CERES boundary fluxes are

363   desired to compute CACK), the uncertainty related to *physical variability* ($\sigma_{PV}(x_n)$) can be

364   dropped from Eq. (21).

365   *d. Climatological CACK example application*

366   To demonstrate CACK's application when based on monthly CERES EBAF climatology,

367   including the handling of uncertainty, we estimate the annual mean local *ΔF* from a $\Delta\alpha$

368   scenario associated with hypothetical deforestation in the tropics, where *ΔF* for a given month

369   is estimated as Eq. (4) where K_{α_s} is the 2001-2016 monthly climatological CACK and $\Delta\alpha$ is

370   the difference in the 2001-2011 monthly climatological mean white-sky surface albedo

371   between "Croplands" (CRO) and "Evergreen broadleaved forests" (EBF) taken from Gao *et*

372   *al*. (2014) which is based on International Geosphere-Biosphere Program definitions of land

373   cover classification.

374   The monthly climatological albedo look-up maps of Gao *et al*. (2014) contain their own

375   uncertainties, which we take as the mean absolute difference between the monthly albedos

376   reconstructed using their look-up model and the monthly MODIS retrieval record (c.f. Table 3

377   in Gao *et al*. (2014)).

378   The total estimated uncertainty linked to the annual local (i.e., grid cell) instantaneous *ΔF* can

379   thus be expressed (in W m^{-2}) as:

$$\sigma(\Delta F) = \frac{1}{12} \sum_{m=1}^{12} |\Delta F_m| \sqrt{\left(\frac{\sigma(K_{\alpha_s,m})}{K_{\alpha_s,m}} \right)^2 + \left(\frac{\sigma(\Delta \alpha_{s,m})}{\Delta \alpha_{s,m}} \right)^2} \tag{22}$$

where $\sigma(K_{\alpha_s,m})/K_{\alpha_s,m}$ is the relative grid cell uncertainty of CACK and $\sigma(\Delta \alpha_{s,m})/\Delta \alpha_{s,m}$ is

the relative uncertainty of $\Delta \alpha_s$ in month m defined as:

$$\frac{\sigma(\Delta \alpha_{s,m})}{\Delta \alpha_{s,m}} = \sqrt{\left(\frac{\sigma(\alpha_{s,m})}{\alpha_{CRO,m}} \right)^2 + \left(\frac{\sigma(\alpha_{s,m})}{\alpha_{EBF,m}} \right)^2} \tag{23}$$

where $\sigma(\alpha_{s,m})$ is the monthly absolute uncertainty of the climatological mean surface albedo

(i.e., of the Gao *et al*. (2014) product).

e. Temporally-explicit CACK application example

Use of a temporally-explicit CACK may be desirable for time-sensitive applications within

the CERES era. This is particularly true for regions experiencing significant changes to the

atmospheric state affecting shortwave radiation transfer. A good example is in southern

Amazonia where tropical deforestation has been linked to changes in cloud cover (Durieux et

al., 2003; Lawrence and Vandecar, 2014; Wright et al., 2017). To exemplify this, we estimate

the annual mean instantaneous $\varDelta F$ for CERES grid cells in the region having experienced both

significant positive trends in surface albedo and negative trends in cloud area fraction during

the 2001-2016 period. Grid cell trends in surface albedo and cloud area fraction are deemed

significant if the slopes of linear fits obtained from local (i.e., grid cell) ordinary least squares

regressions had p-values ≤ 0.05. We then apply the slope of the surface albedo trend to

represent the monthly mean interannual $\Delta \alpha$ incurred over the time series together with

CACK updated monthly to estimate the local annual mean instantaneous $\varDelta F$ at each step in

the series:

400 $$\Delta F(t) = \sum_{m=1}^{m=12} -K_{\alpha_s, m}(t) \Delta \alpha_s \qquad (24)$$

401 where $K_{\alpha_s, m}(t)$ is the monthly CACK in year t of the time series. ΔF is then averaged across

402 all grid cells in the sample, with the results then compared to the ΔF that is computed for the

403 same grid sample using the time-insensitive CAM5 and ECHAM6 kernels (i.e., $K_{\alpha_s, m} \neq f(t)$).

404 Using the slope of the surface albedo trend as the $\Delta \alpha_s$ for all months and years rather than the

405 actual $\Delta \alpha_{s,m}(t)$ (i.e., $\Delta \alpha_{s,m}(t) = \alpha_{s,m,t} - \alpha_{s,m,t-1}$) yields the same result when averaged over the

406 full time period but allows us to isolate the effect of the changing atmospheric state on

407 calculations of ΔF. We limit the ΔF uncertainty estimate to CACK's uncertainty that includes

408 $\sigma_{DU}(x_n)$ and $\sigma_{ME}(x_n)$ but excludes $\sigma_{PV}(x_n)$.

409 **5. Results**

410 *a. Initial performance screening*

411 Seasonally, differences in latitude band means between the CERES kernel candidates and the

412 multi-GCM mean kernels are shown in Figure 1.

413

414 < Figure 1 >

415

416 Qualitatively, starting with December-January-February (*DJF*), $K_{\alpha_s}^{BO18}$ gives the best

417 agreement with $K_{\alpha_s}^{\overline{GCM}}$ with the exception of the zone around 55 – 65°S (-55 – -65°), where

418 $K_{\alpha_s}^{QH06}$ gives slightly better agreement (Fig. 1A). In March-April-May (*MAM*), $K_{\alpha_s}^{BO18}$ appears

419 to give the best overall agreement with the exception of the high Arctic, where $K_{\alpha_s}^{ANISO}$ and

420 $K_{\alpha_s}^{C12}$ give better agreement, and with the exception of the zone around 60 – 65°S (-60 – -65°)

421 where $K_{\alpha_s}^{QH06}$, $K_{\alpha_s}^{ANISO}$, and $K_{\alpha_s}^{C12}$ agree best with $K_{\alpha_s}^{\overline{GCM}}$ (Fig. 1B). The largest spread in

422   disagreement across all six CERES kernels is found in June-July-August (*JJA*; Fig. 1 C) at

423   northern high latitudes. $K_{\alpha_s}^{BO18}$ appears to agree best both here and elsewhere with the

424   exception of the zone between ~20 – 35°N, where $K_{\alpha_s}^{QH06}$ gives slightly better agreement.

425   In September-October-November (*SON*), $K_{\alpha_s}^{BO18}$ agrees best with $K_{\alpha_s}^{\overline{GCM}}$ at all latitudes except

426   the zone between 10 – 25°N and 55 – 65°S where $K_{\alpha_s}^{QH06}$ agrees slightly better.

427   Quantitatively, the proportion of the total variance explained by linear regressions of monthly

428    $K_{\alpha_s}^{\overline{GCM}}$ on monthly $K_{\alpha_s}^{CERES}$ (i.e., "R^2") is highest and equal for the CERES kernels based on the

429   ANISO, QH06, and BO18 models (Fig. 2 B, C, & D). Of these three, $K_{\alpha_s}^{QH06}$ has a y-intercept

430   ("B_0") closest to 0 and a slope ("*m*") of 1, although the root mean squared error ("*RMSE*") –

431   an accuracy measure – is slightly better (lower) for $K_{\alpha_s}^{BO18}$. The two CERES kernels with the

432   lowest R^2, highest slopes (negative deviations), highest *RMSE*s, and y-intercepts with the

433   largest absolute difference from zero – or the worst performing candidates – are those based

434   on the ISO and M10 models (Fig. 2 A&E).

435

436   < Figure 2 >

437

438   Although the y-intercept deviation from 0 for $K_{\alpha_s}^{C12}$ is relatively low, its *RMSE* is ~50%

439   higher than that of $K_{\alpha_s}^{QH06}$, $K_{\alpha_s}^{BO18}$, and $K_{\alpha_s}^{ANISO}$ and leads to notable positive deviation from the

440   multi-GCM mean ($K_{\alpha_s}^{\overline{GCM}}$) judging by its slope of 0.92.

441   Globally, *NAD* for the QH06, ANISO, and BO18 kernels are far superior to the ISO, M10,

442   and C12 kernels (Table 3).

443

444   < Table 3 >

445

446   After filtering to remove grid cells for oceans and other water bodies, *NAD* scores for these

447   three kernels decreased; the decrease was smallest for $K_{\alpha_s}^{BO18}$ (-0.03) and largest for $K_{\alpha_s}^{QH06}$ (-

448   0.06). Despite constraining the analysis to land surfaces only, the rank order remained

449   unchanged (Table 3), and $K_{\alpha_s}^{QH06}$, $K_{\alpha_s}^{BO18}$, and $K_{\alpha_s}^{ANISO}$ are subjected to further evaluation.

450   *b. GCM kernel emulation and additional performance evaluation*

451   However, because the QH06 model ($K_{\alpha_s}^{QH06}$) required auxiliary inputs for cloud cover area

452   fraction and cloud optical depth – two atmospheric state variables not provided with the

453   ECHAM6 and CAM5 kernel datasets – it was not possible to emulate these two GCM kernels

454   with $K_{\alpha_s}^{QH06}$. Additional performance evaluation through GCM kernel emulation is therefore

455   restricted to the ANISO and BO18 models.

456   < Figure 3 >

457   Globally, the kernel based on the ANISO model displays larger annual mean biases relative to

458   BO18 when compared to both ECHAM6 and CAM5 kernels (Figure 3). Notable positive

459   biases over land with respect to both ECHAM6 and CAM5 kernels are evident in the northern

460   Andes region of South America, the Tibetan plateau, and the tropical island region comprising

461   Indonesia, Malaysia, and Papua New Guinea (Fig. 3 A & C). Notable negative biases over

462   land with respect to both ECHAM6 and CAM5 kernels are evident over Greenland,

463   Antarctica, northeastern Africa, and the Arabian Peninsula (Fig. 3 A & C).

464   < Figure 4 >

465   Globally, annual biases for BO18 are generally found to be lower than for ANISO and are

466   mostly non-existent in extra-tropical ocean regions (Fig. 3 B & D). Patterns in biases over

467   land are mostly negative with the exception of Saharan Africa where the annual mean bias

468   with respect to both GCMs is positive. For BO18, systematic positive biases – or biases

469   evident with respect to both GCM kernels – appear over eastern tropical and subtropical

470   marine coastal upwelling zones where marine stratocumulus cloud dynamics are difficult for

471   GCMs to resolve (Bretherton et al., 2004; Richter, 2015).

472   < Table 4 >

473   Regression statistics (Figure 4) indicate a greater overall performance for BO18 than for

474   ANISO. RMSEs for monthly kernels emulated with BO18 are 9.0 and 8.2 W m^{-2} for CAM5

475   and ECHAM6, respectively – which is ~50-60% of the RMSEs emulated with the ANISO

476   model. Relative to ANISO, the BO18 model also gives a higher R^2, a slope closer to 1, and a

477   y-intercept closer to zero (Figure 4). The BO18 model (or parameterization) is therefore

478   selected for the CERES albedo change kernel (CACK).

479   Focusing only on the GCM kernels emulated with $K_{\alpha_s}^{BO18}$ henceforth, global mean negative

480   biases are evident in all months (Table 4), with the largest biases (in magnitude) appearing in

481   May (-4.4 W m^{-2}) and November (-2.5 W m^{-2}) for CAM5 and ECHAM6, respectively. In

482   absolute terms, largest biases of 8.6 W m^{-2} and 6.8 W m^{-2} appear in June for CAM5 and

483   ECHAM6, respectively. Annually, the mean absolute bias for CAM5 and ECHAM6 is 6.8

484   and 6.1 W m^{-2}, respectively – a magnitude which seems remarkably low if one compares this

485   to the annual mean disagreement (standard deviation) of 33 W m^{-2} across all four GCM

486   kernels (not shown; for seasonal mean standard deviations see Fig. 1).

487   *c. CACK uncertainty*

488   For a kernel based on 2001-2016 monthly mean CERES EBAF climatology, Figure 5

489   illustrates the contribution of the absolute error related to $K_{\alpha_s}^{BO18}$'s model form (Fig. 5 A,

490 annual mean) relative to CACK's total absolute uncertainty (Fig. 5 C, annual mean), which

491 includes the uncertainty surrounding CERES EBAF v4 input variables $SW_\downarrow^{SFC}$ and $SW_\downarrow^{TOA}$

492 and their interannual variability (Fig. 5 B, annual mean).

493 < Figure 5 >

494 Total propagated σ_{pv} and σ_{du} far exceeds σ_{me}, is dominated by $\sigma_{du}(SW_\downarrow^{SFC})$ and

495 $\sigma_{pv}(SW_\downarrow^{SFC})$, and is largest in the Pacific region to the south of the intertropical convergence

496 zone (ITCZ). Over land, the annual σ_{pv} and σ_{du} as well as the annual σ_{total} are generally

497 largest in arid or high altitude regions (Fig. 5 B). However, annual CACK values are also

498 large in these regions reducing the relative uncertainty (Fig. 5 D). The largest relative

499 uncertainties over land (on an annual basis) – which can approach 50% – are found over

500 central Europe, northwestern Asia, southeastern China, Andean Chile, and northwestern N.

501 America (Fig. 5 D).

502 *d. Climatological CACK application*

503 When estimated with a CACK based on monthly CERES EBAF climatology, the annual local

504 *ΔF* from $\Delta\alpha_s$ linked to hypothetical deforestation in the tropics is negative in most regions,

505 approaching -20 W m^{-2} locally in some regions of the Brazilian Cerrado and south of the

506 Sahel region in Africa (Fig. 6 B). The combined CACK and $\Delta\alpha_s$ uncertainty for these

507 regions can approach $\pm$ 5 W m^{-2} annually (Fig. 6 C) in regions like the Brazilian Cerrado and

508 sub-Sahel Africa. Relative to the *ΔF* magnitude, however, the largest uncertainties (annual)

509 may be found in the subtropical regions of Central America, southern Brazil, southern Asia,

510 and northern Australia, where it can approach 30-40% (Fig. 6 D).

511 *e. Temporally-explicit CACK application*

512   The effect of a decreasing cloud cover and increasing surface albedo trend in southern

513   Amazonia (Fig. 7 B) on shortwave radiative transfer and thus a CACK-based estimate of

514   regional mean annual ΔF emerges in Figure 7 C, where ΔF increases in magnitude by 0.004

515   W m^{-2} from 2002 to 2016. This ΔF trend would otherwise go undetected if a GCM-based

516   kernel were applied to the same surface albedo trend – that is, to a sustained positive

517   interannual monthly albedo change "pulse". Alternatively, a CACK based on 2001 CERES

518   EBAF inputs (applied with $\Delta \alpha_s$ for 2001-2002) would give slightly higher ΔF estimates

519   relative to those based on ECHAM6 and CAM5 kernels; conversely, a CACK based on 2015

520   CERES EBAF inputs (applied with $\Delta \alpha_s$ for 2015-2016) that would yield lower ΔF estimates

521   relative to those based on the same two GCM-based kernels (Fig. 7 C). Use of temporally-

522   explicit CACK can therefore capture ΔF trends related to a changing atmospheric state that

523   fixed-state GCM kernels are unable to capture.

524   **5. Discussion**

525   Motivated by an increasing abundance of climate impact research focusing on land processes

526   in recent years, we comprehensively evaluated six simplified models (or parameterizations) as

527   candidates for an albedo change kernel based on the CERES EBAF v4 products (Kato et al.,

528   2018; Loeb et al., 2017). Relative to albedo change kernels based on sophisticated radiative

529   transfer schemes embedded in GCMs, a CERES-based albedo change kernel – or CACK –

530   represents a more transparent and empirically-rooted alternative that can be updated

531   frequently at relatively low cost. This allows greater flexibility to meet the needs of research

532   focusing on surface albedo trends within the CERES era in regions currently undergoing rapid

533   changes to atmospheric state as it affects shortwave radiation transfer. Although some

534   modeling groups have provided recent updates to their albedo change kernels using the latest

535   GCM versions (e.g., (Pendergrass et al., 2018)), the atmospheric state conditions used to

536   derive them may still be considered outdated or not in sync with that required for many

537   applications (Table 1).

538   Based on both qualitative and quantitative benchmarking against the mean of four GCM

539   kernels, the novel kernel parameterization obtained from machine learning $K_{\alpha_s}^{BO18}$, together

540   with the two (semi-)analytically derived kernels $K_{\alpha_s}^{QH06}$ and $K_{\alpha_s}^{ANISO}$, proved far superior to the

541    $K_{\alpha_s}^{ISO}$ analytical kernel and to the two additional empirical parameterizations $K_{\alpha_s}^{C12}$ and $K_{\alpha_s}^{M10}$.

542   When subjected to additional performance evaluation, however, we found that $K_{\alpha_s}^{BO18}$ was

543   able to more robustly emulate two GCM kernels (ECHAM6 and CAM5) with exceptionally

544   high agreement, suggesting that $K_{\alpha_s}^{BO18}$ could serve as a suitable candidate for CACK.

545   Relative to the monthly CAM5 and ECHAM6 kernels, the mean absolute monthly emulation

546   "error" of $K_{\alpha_s}^{BO18}$ was found to be 6.8 and 6.1 W m^{-2}, respectively – a magnitude which is only

547   ~20% of the standard deviation found across four GCM kernels (annual mean). CACK's

548   remarkable simplicity lends support to the idea of using machine learning to explore and

549   detect emergent properties of radiative transfer or other complex, interactive model outputs in

550   future research. The fact that the $K_{\alpha_s}^{BO18}$ parameterization emerged as the best common

551   solution from two independently executed machine learning analyses each employing a

552   random sampling unique to a specific GCM kernel suggests that the $K_{\alpha_s}^{BO18}$ parameterization is

553   robust and insensitive to the underlying GCM representation of shortwave radiative transfer.

554   Despite its stronger empirical foundation over a GCM-based kernel, it is important to

555   recognize CACK's limitations. Firstly, while CACK has a finer spatial resolution than most

556   GCM kernels, it still represents a spatially averaged response rather than a truly local

557   response; in other words, the state variables used to define the $SW_{\uparrow}^{TOA}$ response are averages

558 tied to the coarse spatial (i.e., 1° x 1°) resolution of the CERES EBAF v4 product grids.

559 Secondly, the monthly CERES EBAF-Surface product used to define lower atmospheric

560 boundary conditions is not strictly an observation. The space-borne platform is not able to

561 directly observe surface irradiances, requiring additional satellite-based estimates of cloud and

562 aerosol properties as input to a radiative transfer model (Kato et al., 2012). Although TOA

563 irradiances are applied to constrain the surface irradiances, they remain susceptible to errors

564 in the radiative transfer model inputs. Considering this error as "data uncertainty" increases

565 CACK's overall uncertainty beyond that which is related to its underlying parameterization or

566 "model error". The uncertainty of CERES surface shortwave irradiances as well as extensive

567 ground validation and testing are documented in greater detail elsewhere (Kato et al., 2013;

568 Kato et al., 2018; Loeb et al., 2017; Loeb et al., 2009) and may continue to be reduced in

569 future EBAF-Surface versions.

570 *Concluding remarks*

571 To conclude, we developed, evaluated, and proposed a radiative kernel for surface albedo

572 change based on CERES EBAF v4 products – or CACK. Relative to existing kernels based on

573 GCMs, CACK provides a higher spatial resolution, higher transparency alternative that is

574 more amenable to user needs. For LULCC research of the near-past, present day, or near-

575 future periods, application of a CACK whose inputs are based on monthly climatological

576 means of the full CERES EBAF record can better-account for the corresponding interannual

577 variability in Earth's atmospheric state affecting shortwave radiative transfer. For regions

578 undergoing changes in atmospheric state that are detectable above the normal variability

579 within the CERES era, application of a temporally-explicit CACK can better-account for its

580 influence on ΔF estimates from surface albedo change. CACK's input flexibility and

581 transparency combined with documented uncertainty make it well-suited to be applied as part

582   of a Monitoring, Reporting, and Verification (MRV) framework for biogeophysical impacts

583   on land, analogous to those which currently exist for land sector greenhouse gas emissions.

584

585   **Code and Dataset Availability**

586   We make both monthly temporally-explicit and monthly climatological mean CACKs for

587   years 2001-2016 available as a complete data product ("CACKv1.0"; netCDF file available at

588   doi:10.6073/pasta/d77b84b11be99ed4d5376d77fe0043d8) that includes their respective

589   uncertainty layers. A summary of this dataset and associated variables is provided in Table

590   S3 of the Supporting Information. Octave script files for generating monthly CACK and

591   demonstrating its application with user-specified temporal and spatial extents are bundled

592   with the netCDF file.

593

594   **Data Availability**

595   CERES EBAF data are available for download at:

596   https://ceres.larc.nasa.gov/products.php?product=EBAF-TOA . The CAM3 kernel is

597   available at: http://people.oregonstate.edu/~shellk/kernel.html . The CAM5 kernel is

598   available at: https://www.earthsystemgrid.org/ac/guest/secure/sso.html . The ECHAM5

599   kernel is available at: https://swiftbrowser.dkrz.de/public/dkrz_0c07783a-0bdc-4d5e-9f3b-

600   c1b86fac060d/Radiative_kernels/ .

601

602   **Acknowledgements**

603   R.M.B. was supported by the Research Council of Norway, grants #244074/E20 and

604   #250113/F20; T.L.O. was supported by the Climate and Land Use program award #2017-

605   68002-26612 of the USDA National Institute of Food and Agriculture.

606

610 **References**

611 Anav, A., Friedlingstein, P., Kidston, M., Bopp, L., Ciais, P., Cox, P., Jones, C., Jung, M., Myneni, R.,
612   and Zhu, Z.: Evaluating the Land and Ocean Components of the Global Carbon Cycle in the
613   CMIP5 Earth System Models, Journal of Climate, 26, 6801-6843, 2013.

615 Atwood, A. R., Wu, E., Frierson, D. M. W., Battisti, D. S., and Sachs, J. P.: Quantifying Climate
616   Forcings and Feedbacks over the Last Millennium in the CMIP5–PMIP3 Models, Journal of
617   Climate, 29, 1161-1178, 2016.

619 Block, K. and Mauritsen, T.: Forcing and feedback in the MPI-ESM-LR coupled model under abruptly
620   quadrupled CO2, Journal of Advances in Modeling Earth Systems, 5, 676-691, 2014.

622 Bonan, G. B., Pollard, D., and Thompson, S. L.: Effects of Boreal Forest Vegetation on Global
623   Climate, Nature, 359, 716-718, 1992.

625 Bozzi, E., Genesio, L., Toscano, P., Pieri, M., and Miglietta, F.: Mimicking biochar-albedo feedback
626   in complex Mediterranean agricultural landscapes, Environmental Research Letters, 10, 084014,
627   2015.

629 Breipohl, A. M.: Probabilistic systems analysis: an introduction to probabilistic models, decisions,
630   and applications of random processes, Wiley, New York, 1970.

632 Bretherton, C. S., Uttal, T., Fairall, C. W., Yuter, S. E., Weller, R. A., Baumgardner, D., Comstock,
633   K., Wood, R., and Raga, G. B.: The Epic 2001 Stratocumulus Study, Bulletin of the American
634   Meteorological Society, 85, 967-978, 2004.

636 Bright, R. M.: Metrics for Biogeophysical Climate Forcings from Land Use and Land Cover Changes
637   and Their Inclusion in Life Cycle Assessment: A Critical Review, Environmental Science &
638   Technology, 49, 3291-3303, 2015.

640 Bright, R. M. and Kvalevåg, M. M.: Technical note: Evaluating a simple parameterization of radiative
641   shortwave forcing from surface albedo change, Atmospheric Chemistry and Physics, 13, 11169-
642   11174, 2013.

644 Caiazzo, F., Malina, R., Staples, M. D., Wolfe, P., J. ,, Yim, S. H. L., and Barrett, S. R. H.:
645   Quantifying the climate impacts of albedo changes due to biofuel production: a comparison with
646   biogeochemical effects, Environmental Research Letters, 9, 024015, 2014.

648 Carrer, D., Pique, G., Ferlicoq, M., Ceamanos, X., and Ceschia, E.: What is the potential of cropland
649   albedo management in the fight against global warming? A case study based on the use of cover
650   crops, Environmental Research Letters, 13, 044030, 2018.

652 CERES Science Team: CERES EBAF-Surface Edition 4.0. NASA Atmospheric Science and Data
653   Center (ASDC). https://doi.org/10.5067/TERRA+AQUA/CERES/EBAF-SURFACE_L3B004.0 .
654   Accessed January 14, 2018., 2018a.

656   CERES Science Team: CERES EBAF-TOA Edition 4.0. NASA Atmospheric Science and Data
657   Center (ASDC). https://doi.org/10.5067/TERRA+AQUA/CERES/EBAF-TOA_L3B004.0 . Accessed
658   January 14, 2018. . 2018b.
659
660   Cherubini, F., Bright, R. M., and Strømman, A. H.: Site-specific global warming potentials of biogenic
661   CO_2 for bioenergy: contributions from carbon fluxes and albedo dynamics, Environmental
662   Research Letters, 7, 045902, 2012.
663
664   Clifford, A. A.: Multivariate error analysis: A handbook of error propagation and calculation in many-
665   parameter systems, Applied Science Publishers, London, U. K., 1973.
666
667   Collins, W. D., Rasch, P. J., Boville, B. A., Hack, J. J., McCaa, J. R., Williamson, D. L., Briegleb, B.
668   P., Bitz, C. M., Lin, S.-J., and Zhang, M.: The Formulation and Atmospheric Simulation of the
669   Community Atmosphere Model Version 3 (CAM3), Journal of Climate, 19, 2144-2161, 2006.
670
671   Dickinson, R. E. and Henderson-Sellers, A.: Modelling tropical deforestation: A study of GCM land-
672   surface parametrizations, Quarterly Journal of the Royal Meteorological Society, 114, 439-462,
673   1988.
674
675   Dolinar, E. K., Dong, X., Xi, B., Jiang, J. H., and Su, H.: Evaluation of CMIP5 simulated clouds and
676   TOA radiation budgets using NASA satellite observations, Clim. Dyn., 44, 2229-2247, 2015.
677
678   Donohoe, A. and Battisti, D. S.: Atmospheric and Surface Contributions to Planetary Albedo, Journal
679   of Climate, 24, 4402-4418, 2011.
680
681   Durieux, L., Machado, L. A. T., and Laurent, H.: The impact of deforestation on cloud cover over the
682   Amazon arc of deforestation, Remote Sensing of Environment, 86, 132-140, 2003.
683   Free, M. and Sun, B.: Trends in U.S. Total Cloud Cover from a Homogeneity-Adjusted Dataset,
684   Journal of Climate, 27, 4959-4969, 2014.
685
686   Gao, F., He, T., Wang, Z., Ghimire, B., Shuai, Y., Masek, J., Schaaf, C., and Williams, C.: Multi-scale
687   climatological albedo look-up maps derived from MODIS BRDF/albedo products, Journal of
688   Applied Remote Sensing, 8, 2014.
689
690   Ghimire, B., Williams, C. A., Masek, J., Gao, F., Wang, Z., Schaaf, C., and He, T.: Global albedo
691   change and radiative cooling from anthropogenic land cover change, 1700 to 2005 based on
692   MODIS, land use harmonization, radiative kernels, and reanalysis, Geophysical Research Letters,
693   41, 9087-9096, 2014.
694
695   Green, P., Gardiner, T., Medland, D., and Cimini, D.: WP2: Guide to uncertainty in measurement and
696   its nomenclature. Version 4.0. , U.K., 212 pp., 2017.
697
698   Hurrell, J. W., Holland, M. M., Gent, P. R., Ghan, S., Kay, J. E., Kushner, P. J., Lamarque, J. F.,
699   Large, W. G., Lawrence, D., Lindsay, K., Lipscomb, W. H., Long, M. C., Mahowald, N., Marsh,
700   D. R., Neale, R. B.,
701   Rasch, P., Vavrus, S., Vertenstein, M., Bader, D., Collins, W. D., Hack, J. J., Kiehl, J., and Marshall,
702   S.: The Community Earth System Model: A Framework for Collaborative Research, Bulletin of
703   the American Meteorological Society, 94, 1339-1360, 2013.
704
705   Iqbal, M.: An introduction to solar radiation, Academic Press Canada, Ontario, CA, 1983.
706
707   Jones, A. D., Calvin, K. V., Collins, W. D., and Edmonds, J.: Accounting for radiative forcing from
708   albedo change in future global land-use scenarios, Climatic Change, 131, 691-703, 2015.
709

710   Kashimura, H., Abe, M., Watanabe, S., Sekiya, T., Ji, D., Moore, J. C., Cole, J. N. S., and Kravitz, B.:
711   Shortwave radiative forcing, rapid adjustment, and feedback to the surface by sulfate
712   geoengineering: analysis of the Geoengineering Model Intercomparison Project G4 scenario,
713   Atmos. Chem. Phys., 17, 3339-3356, 2017.
714   Kato, S., Loeb, N. G., Rose, F. G., Doelling, D. R., Rutan, D. A., Caldwell, T. E., Yu, L., and Weller,
715   R. A.: Surface Irradiances Consistent with CERES-Derived Top-of-Atmosphere Shortwave and
716   Longwave Irradiances, Journal of Climate, 26, 2719-2740, 2012.
717
718   Kato, S., Loeb, N. G., Rose, F. G., Doelling, D. R., Rutan, D. A., Caldwell, T. E., Yu, L., and Weller,
719   R. A.: Surface irradiances consistent with CERES-derived top-of-atmosphere shortwave and
720   longwave irradiances, Journal of Climate, 26, 2719-2740, 2013.
721
722   Kato, S., Rose, F. G., Rutan, D. A., Thorsen, T. J., Loeb, N. G., Doelling, D. R., Huang, X., Smith, W.
723   L., Su, W., and Ham, S.-H.: Surface Irradiances of Edition 4.0 Clouds and the Earth's Radiant
724   Energy System (CERES) Energy Balanced and Filled (EBAF) Data Product, Journal of Climate,
725   31, 4501-4527, 2018.
726
727   Lacis, A. A. and Hansen, J. E.: A parameterization for the absorption of solar radiation in the earth's
728   atmosphere, Journal of Atmospheric Sciences, 31, 118-133, 1974.
729
730   Lawrence, D. and Vandecar, K.: Effects of tropical deforestation on climate and agriculture, Nature
731   Climate Change, 5, 27, 2014.
732
733   Lenton, T. M. and Vaughan, N. E.: The radiative forcing potential of different climate geoengineering
734   options, Atmospheric Chemistry and Physics 9, 5539-5561, 2009.
735
736   Li, J. L. F., Waliser, D. E., Stephens, G., Lee, S., L'Ecuyer, T., Kato, S., Loeb, N., and Ma, H.-Y.:
737   Characterizing and understanding radiation budget biases in CMIP3/CMIP5 GCMs, contemporary
738   GCM, and reanalysis, Journal of Geophysical Research: Atmospheres, 118, 8166-8184, 2013.
739
740   Loeb, N. G., Doelling, D. R., Wang, H., Su, W., Nguyen, C., Corbett, J. G., Liang, L., Mitrescu, C.,
741   Rose, F. G., and Kato, S.: Clouds and the Earth's Radiant Energy System (CERES) Energy
742   Balanced and Filled (EBAF) Top-of-Atmosphere (TOA) Edition-4.0 Data Product, Journal of
743   Climate, 31, 895-918, 2017.
744
745   Loeb, N. G., Wielicki, B. A., Doelling, D. R., Smith, G. L., Keyes, D. F., Kato, S., Manalo-Smith, N.,
746   and Wong, T.: Toward optimal closure of the Earth's top-of-atmosphere radiation budget, Journal
747   of Climate, 22, 748-766, 2009.
748
749   Lutz, D. A., Burakowski, E. A., Murphy, M. B., Borsuk, M. E., Niemiec, R. M., and Howarth, R. B.:
750   Tradeoffs between three forest ecosystem services across the state of New Hampshire, USA:
751   timber, carbon, and albedo, Ecological Applications, 26, 146-161, 2015.
752
753   Lutz, D. A. and Howarth, R. B.: The price of snow: albedo valuation and a case study for forest
754   management, Environmental Research Letters, 10, 064013, 2015.
755
756   Mahadevan, S. and Sarkar, S.: Uncertainty analysis methods, U.S. Department of Energy,
757   Washington, D.C., USA, 32 pp., 2009.
758
759   Muñoz, I., Campra, P., and Fernández-Alba, A. R.: Including CO2-emission equivalence of changes in
760   land surface albedo in life cycle assessment. Methodology and case study on greenhouse
761   agriculture, International Journal of Life Cycle Assessment, 15, 672-681, 2010.
762

763 O'Halloran, T. L., Law, B. E., Goulden, M. L., Wang, Z., Barr, J. G., Schaaf, C., Brown, M., Fuentes,
764   J. D., Göckede, M., Black, A., and Engel, V.: Radiative forcing of natural forest disturbances,
765   Global Change Biology, 18, 555-565, 2012.
766 Pendergrass, A. G., Conley, A., and Vitt, F. M.: Surface and top-of-atmosphere radiative feedback
767   kernels for CESM-CAM5, Earth Syst. Sci. Data, 10, 317-324, 2018.
768
769 Qu, X. and Hall, A.: Assessing Snow Albedo Feedback in Simulated Climate Change, Journal of
770   Climate, 19, 2617-2630, 2006.
771
772 Randerson, J. T., Liu, H., Flanner, M. G., Chambers, S. D., Jin, Y., Hess, P. G., Pfister, G., Mack, M.
773   C., Treseder, K. K., Welp, L. R., Chapin, F. S., Harden, J. W., Goulden, M. L., Lyons, E., Neff, J.
774   C., Schuur, E. A. G., and Zender, C. S.: The Impact of Boreal Forest Fire on Climate Warming,
775   Science, 314, 1130-1132, 2006.
776
777 Rasool, S. I. and Schneider, S. H.: Atmospheric Carbon Dioxide and Aerosols: Effects of Large
778   Increases on Global Climate, Science, 173, 138-141, 1971.
779
780 Richter, I.: Climate model biases in the eastern tropical oceans: causes, impacts and ways forward,
781   Wiley Interdisciplinary Reviews: Climate Change, 6, 345-358, 2015.
782
783 Schmidt, M. and Lipson, H.: Distilling free-form natural laws from experimental data, Science, 324,
784   81-85, 2009.
785
786 Schmidt, M. and Lipson, H.: Symbolic regression of implicit equations. In: Genetic Programming
787   Theory and Practice VII, Springer, 2010.
788
789 Shell, K. M., Kiehl, J. T., and Shields, C. A.: Using the Radiative Kernel Technique to Calculate
790   Climate Feedbacks in NCAR's Community Atmospheric Model, Journal of Climate, 21, 2269-
791   2282, 2008.
792
793 Smits, G. F. and Kotanchek, M.: Pareto-front exploitation in symbolic regression. In: Genetic
794   programming theory and practice II, Springer, 2005.
795
796 Soden, B. J., Held, I. M., Colman, R., Shell, K. M., Kiehl, J. T., and Shields, C. A.: Quantifying
797   Climate Feedbacks Using Radiative Kernels, Journal of Climate, 21, 3504-3520, 2008.
798
799 Srivastava, R.: Trends in aerosol optical properties over South Asia, International Journal of
800   Climatology, 37, 371-380, 2017.
801
802 Stephens, G. L., O'Brien, D., Webster, P. J., Pilewski, P., Kato, S., and Li, J.-l.: The albedo of Earth,
803   Reviews of Geophysics, 53, 141-163, 2015.
804
805 Stevens, B., Giorgetta, M., Esch, M., Mauritsen, T., Crueger, T., Rast, S., Salzmann, M., Schmidt, H.,
806   Bader, J., Block, K., Brokopf, R., Fast, I., Kinne, S., Kornblueh, L., Lohmann, U., Pincus, R.,
807   Reichler, T., and Roeckner, E.: Atmospheric component of the MPI-M Earth System Model:
808   ECHAM6, Journal of Advances in Modeling Earth Systems, 5, 146-172, 2013.
809
810 Taylor, K. E., Crucifix, M., Braconnot, P., Hewitt, C. D., Doutriaux, C., Broccoli, A. J., Mitchell, J. F.
811   B., and Webb, M. J.: Estimating Shortwave Radiative Forcing and Response in Climate Models,
812   Journal of Climate, 20, 2530-2543, 2007.
813
814 The GFDL Global Atmospheric Model Development Team: The New GFDL Global Atmosphere and
815   Land Model AM2–LM2: Evaluation with Prescribed SST Simulations, Journal of Climate, 17,
816   4641-4673, 2004.
817

818 Vanderhoof, M., Williams, C. A., Ghimire, B., and Rogan, J.: Impact of mountain pine beetle
819   outbreaks on forest albedo and radiative forcing, as derived from Moderate Resolution Imaging
820   Spectroradiometer, Rocky Mountains, USA, Journal of Geophysical Research: Biogeosciences,
821   118, 1461-1471, 2013.
822
823 Wang, H. and Su, W.: Evaluating and understanding top of the atmosphere cloud radiative effects in
824   Intergovernmental Panel on Climate Change (IPCC) Fifth Assessment Report (AR5) Coupled
825   Model Intercomparison Project Phase 5 (CMIP5) models using satellite observations, Journal of
826   Geophysical Research: Atmospheres, 118, 683-699, 2013.
827
828 Winton, M.: Simple optical models for diagnosing surface-atmosphere shortwave interactions, Journal
829   of Climate, 18, 3796-3806, 2005.
830
831 Winton, M.: Surface Albedo Feedback Estimates for the AR4 Climate Models, Journal of Climate, 19,
832   359-365, 2006.
833
834 Wright, J. S., Fu, R., Worden, J. R., Chakraborty, S., Clinton, N. E., Risi, C., Sun, Y., and Yin, L.:
835   Rainforest-initiated wet season onset over the southern Amazon, Proceedings of the National
836   Academy of Sciences, doi: 10.1073/pnas.1621516114, 2017. 201621516, 2017.
837
838 Zhao, D., Xin, J., Gong, C., Wang, X., Ma, Y., and Ma, Y.: Trends of Aerosol Optical Properties over
839   the Heavy Industrial Zone of Northeastern Asia in the Past Decade (2004–15), Journal of the
840   Atmospheric Sciences, 75, 1741-1754, 2018.
841

842 **Table 1.** Attributes of existing GCM kernels, all of which having a monthly temporal
843 resolution.

Kernel	Base climatology extent	Base climatology period	Shortwave Radiative transfer	Horizontal Resolution	References
ECHAM6	1,000 years	Preindustrial*	RRTM-G	$1.88° \times 1.88°$	(Block and Mauritsen, 2014; Stevens et al., 2013)
CAM3	6 years	1995-2000	δ-Eddington	$1.4° \times 1.4°$	(Collins et al., 2006; Shell et al., 2008)
CAM5	1 year	2006-2007	RRTM-G	$0.94° \times 1.25°$	(Pendergrass et al., 2018)
GFDL	17 years	1979-1995	Exponential sum-fits, 18 bands	$2° \times 2.5°$	(Soden et al., 2008; The GFDL Global Atmospheric Model Development Team, 2004)

844 *Atmospheric CO_2 concentration = 284.7 ppmv; Exact time period unknown

845

846

847 **Table 2**. Definition of CERES input variables and other system optical properties derived

848 from CERES inputs. All variables have a monthly temporal resolution and a spatial

849 resolution of $1° \times 1°$.

CERES EBAF v.4 Shortwave Boundary Fluxes

$SW_\downarrow^{TOA}$	Downwelling solar flux at top-of-atmosphere	Wm^{-2}
$SW_\downarrow^{SFC}$	Downwelling solar flux at surface	Wm^{-2}
$SW_{\downarrow,CLR}^{SFC}$	Clear-sky downwelling solar flux at surface	Wm^{-2}
$SW_\uparrow^{TOA}$	Upwelling solar flux at top-of-atmosphere	Wm^{-2}
$SW_\uparrow^{SFC}$	Upwelling solar flux at surface	Wm^{-2}

System Optical Properties

$T = SW_\downarrow^{SFC} / SW_\downarrow^{TOA}$	Clearness index	unitless
$\alpha_p = SW_\uparrow^{TOA} / SW_\downarrow^{TOA}$	Planetary albedo	unitless
$\alpha_s = SW_\uparrow^{SFC} / SW_\downarrow^{SFC}$	Surface albedo	unitless
$A_p = 1 - \alpha_p$	Effective planetary absorption	unitless
$A_s = \left[SW_\downarrow^{SFC} - SW_\uparrow^{SFC} \right] / SW_\downarrow^{TOA}$	Effective surface absorption	unitless
$A_a = A_p - A_s$	Effective atmospheric absorption	unitless
$T_a = 1 - A_a$	Effective atmospheric transmission	unitless
$T_{a,CLR} = 1 - A_{a,CLR}$	Clear-sky effective atmospheric transmission	unitless
τ	Cloud visible optical depth	unitless
c	Cloud area fraction	fraction

850

851

852   **Table 3.** Normalized absolute deviation and CERES kernel model candidate ranking.

	Global		Land only		
	NAD	Rank	*NAD*	Rank	Mean Rank
ISO	0.05	6	0.05	6	*6*
ANISO	0.64	3	0.59	3	*3*
C12	0.45	4	0.47	4	*4*
M10	0.26	5	0.34	5	*5*
QH06	0.66	2	0.60	2	*2*
BO18	0.67	1	0.64	1	*1*

853

854

Table 4. Global monthly mean bias (*MB*) and mean absolute bias (*MAB*) for K_α^{BO18} emulated with T and $SW_\downarrow^{SFC}$ from ECHAM6 and CAM5. For reference, the global mean value of K_α^{BO18} is 133 W m^{-2}.

	Jan.	Feb.	Mar.	Apr.	May	Jun.	Jul.	Aug.	Sep.	Oct.	Nov.	Dec.	Ann.
					MB (W m^{-2})								
$K_\alpha^{BO18} - K_\alpha^{CAM5}$	-2.9	-3.4	-3.3	-3.9	-4.4	-3.8	-3.8	-3.7	-3.4	-3.8	-3.7	-3.3	-3.6
$K_\alpha^{BO18} - K_\alpha^{ECHAM6}$	-1.9	-2.2	-1.8	-1.9	-2.2	-1.5	-1.1	-1.6	-1.7	-2.5	-2.5	-1.8	-1.9
					MAB (W m^{-2})								
$\|K_\alpha^{BO18} - K_\alpha^{CAM5}\|$	6.9	5.7	5.2	6.8	7.7	8.6	7.9	6.7	5.6	6.1	6.9	6.9	6.8
$\|K_\alpha^{BO18} - K_\alpha^{ECHAM6}\|$	6.3	5.7	5.0	5.9	6.7	6.8	6.4	5.8	5.3	5.6	6.4	6.7	6.1

855
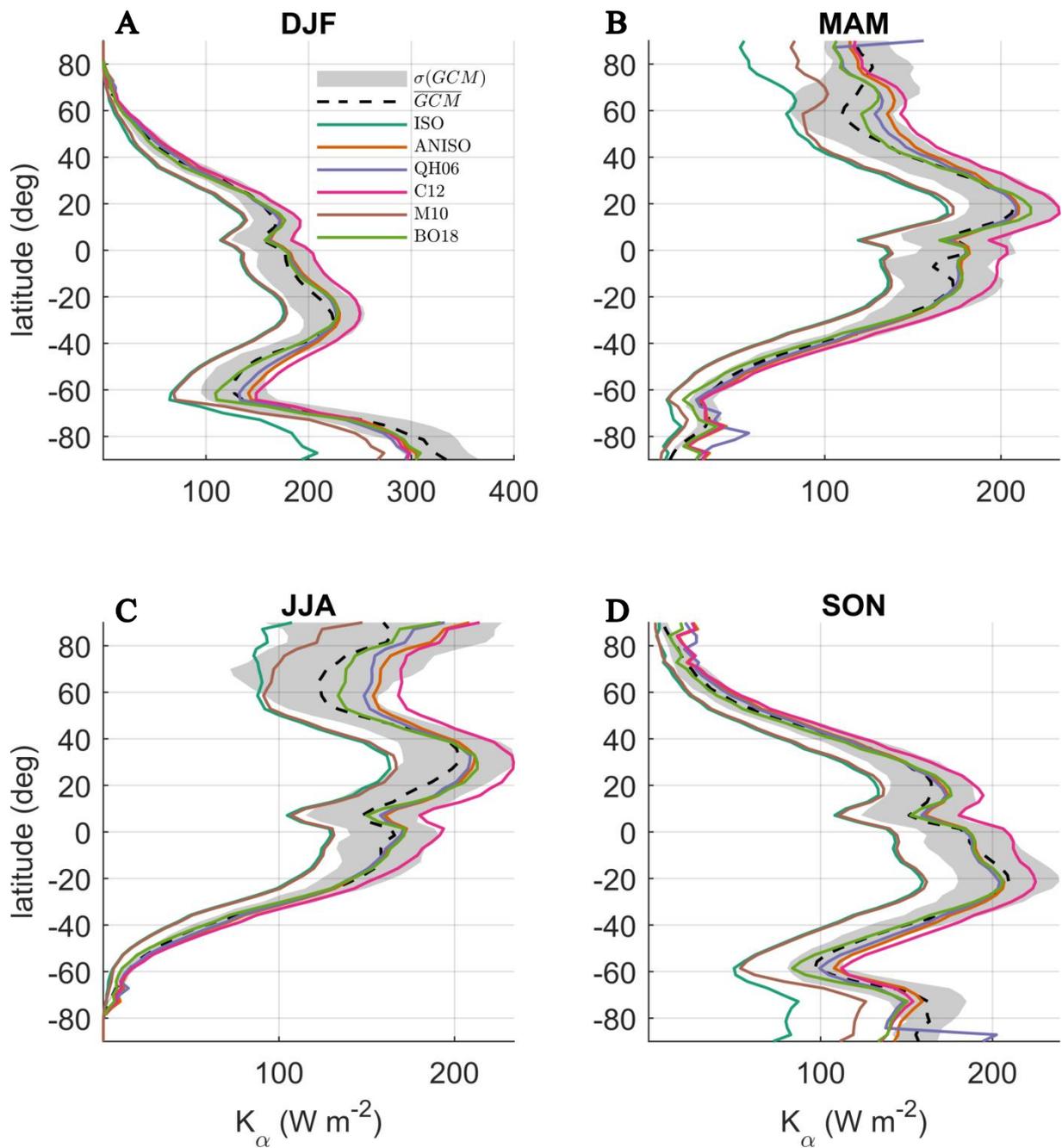
Figure 1. Latitudinal (1°) and seasonal means of the multi-GCM mean ($K_\alpha^{\overline{GCM}}$) and CACK model candidates for: A) December-January-February (DJF); B) March-April-May (MAM); C) June-July-August (JJA); D) September-October-November (SON). CACK model candidates refer to those presented in section 3 and not to those of the model selection phase of the machine learning algorithm.
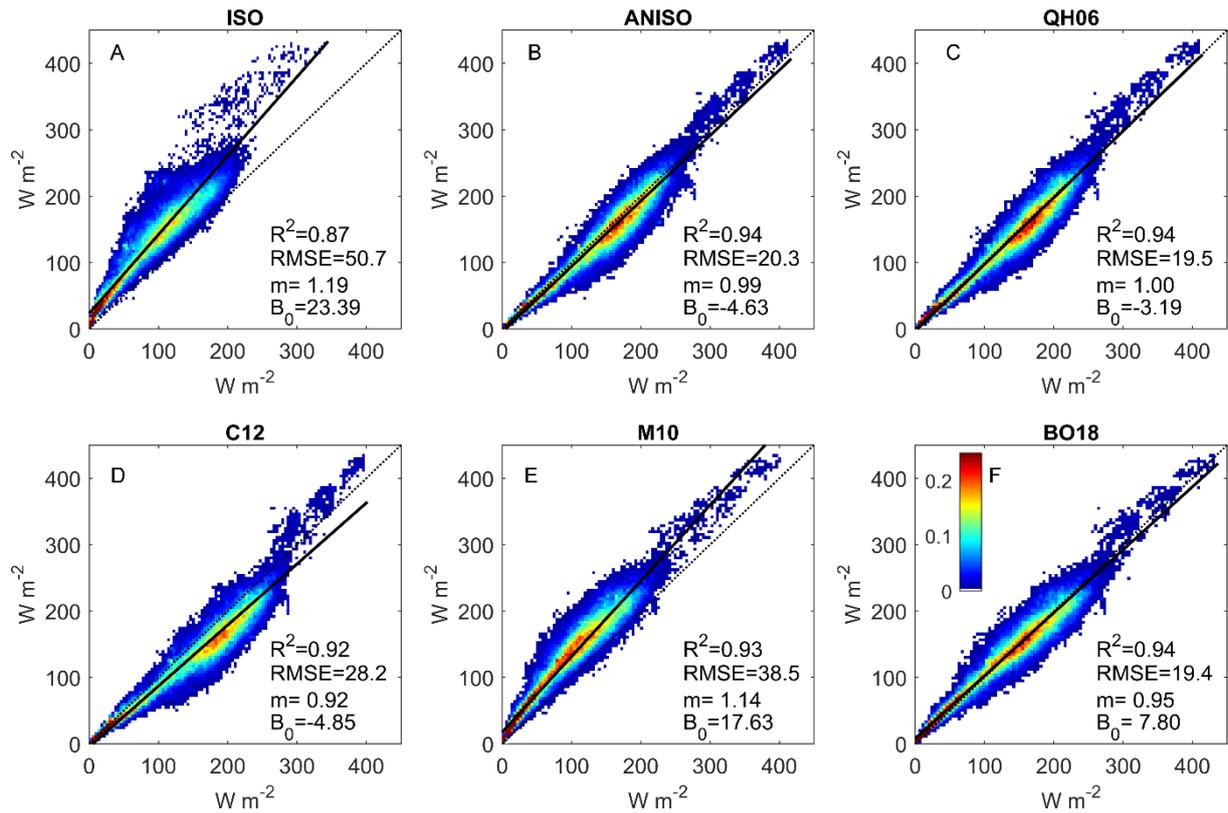
Figure 2. A)-F): Scatter-density regressions of global monthly mean $K_\alpha^{\overline{GCM}}$ (y-axis) and K_α^{CERES} (x-axis), with the CERES kernel identifier shown at the top of each sub-panel. "*m*" = slope; "B_0" = y-intercept. The color scale indicates the percentage of regression points that fall within an averaging bin, where the x-axis and y-axis have been gridded into 100×100 equally-spaced bins to help illustrate the density of overlapping points.

870
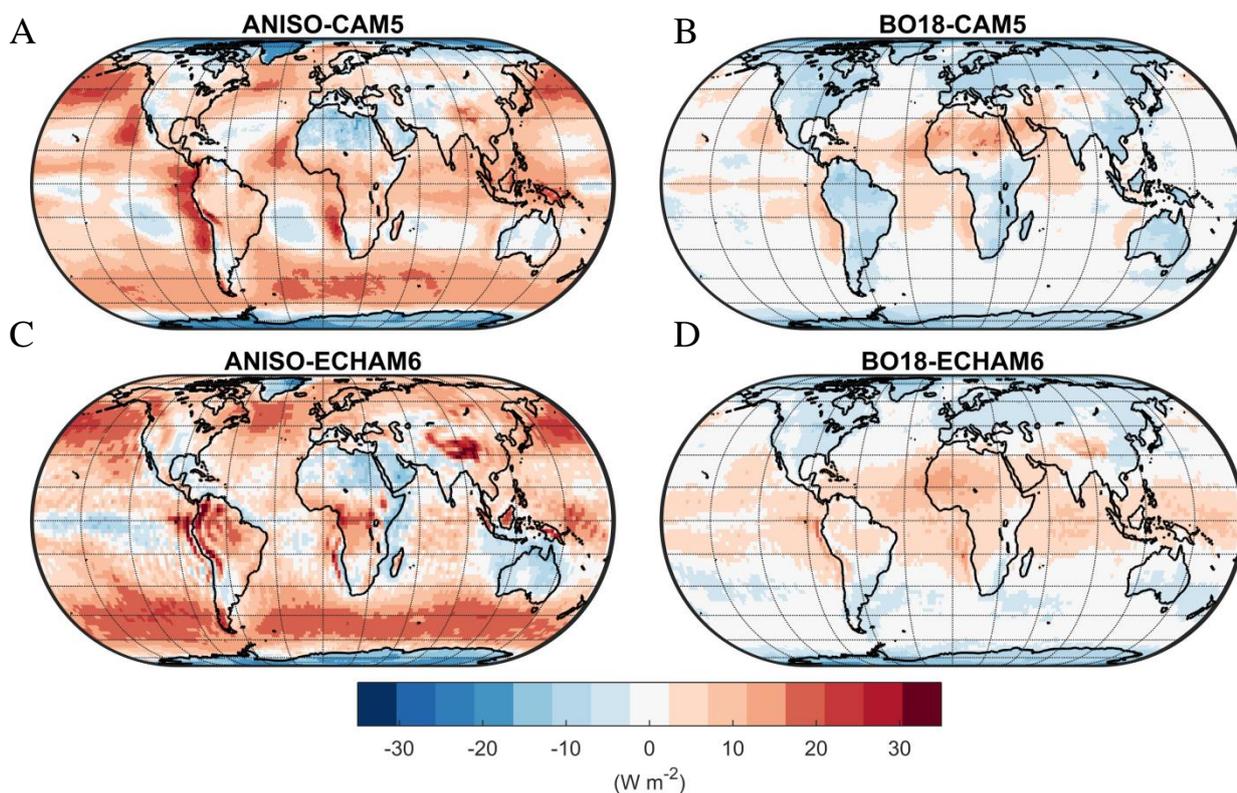
Figure 3. A) Mean annual bias of the CAM5 albedo change kernel emulated with the ANISO

semi-empirical model; B) Mean annual bias of the CAM5 albedo change kernel emulated

with the BO18 parameterization; C) Mean annual bias of the ECHAM6 albedo change kernel

emulated with the ANISO semi-empirical model; D) Mean annual bias of the ECHAM6

albedo change kernel emulated with the BO18 parameterization

876
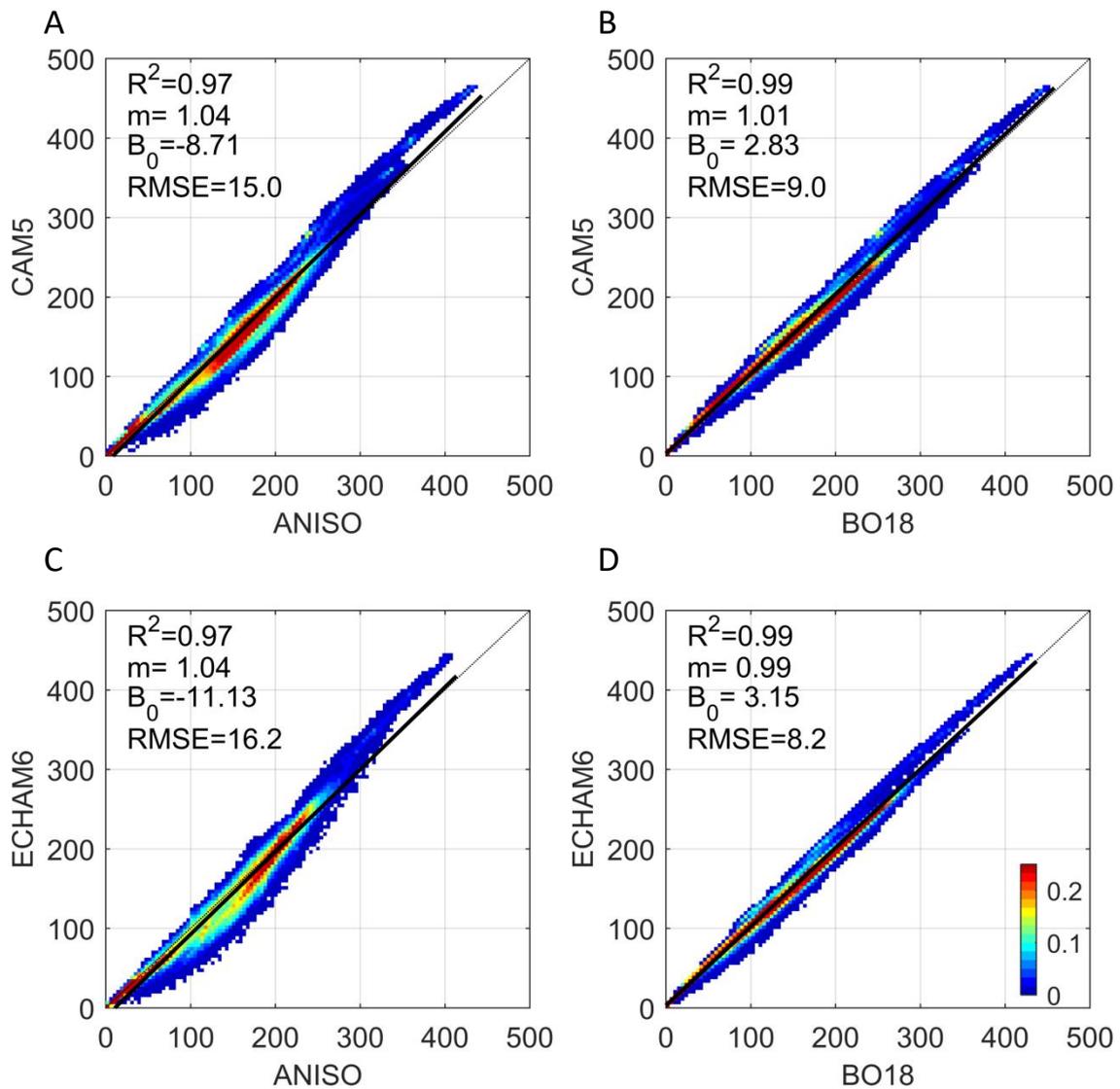
Figure 4. A)-D): Scatter-density regressions of K_α^{GCM} (y-axis) and K_α^{GCM} emulated with the ANISO semi-empirical model and BO18 parameterization (x-axis); "m" = slope; "B_0" = y-intercept. See Figure 2 caption for a description of the color scale.
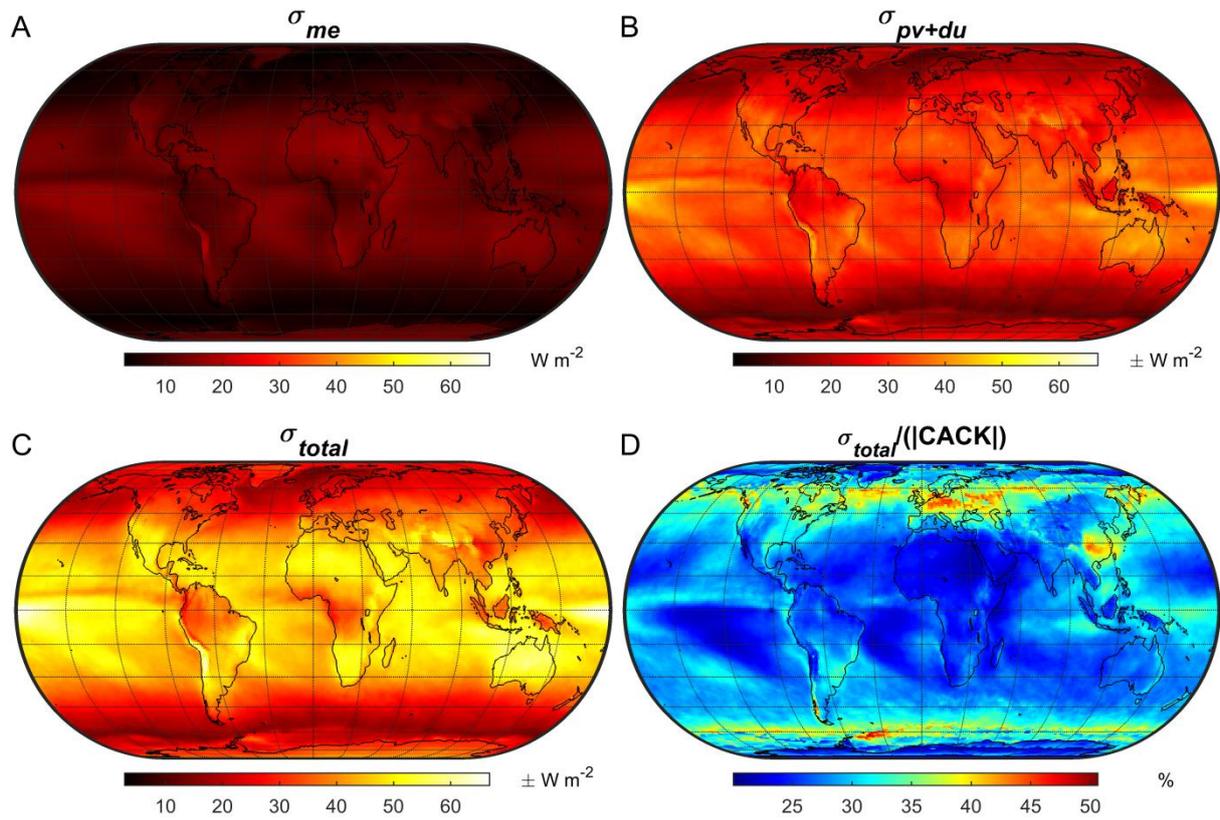
Figure 5. Annual uncertainty of a CACK based on 2001-2016 monthly mean CERES EBAF

v4 climatology: A) The absolute uncertainty related to *model error* (i.e., the $K_{\alpha_s}^{BO18}$

parameterization); B) The total propagated absolute uncertainty related to *physical variability*

and *data uncertainty* of CACK input variables; C) Total absolute uncertainty; D) Total

relative uncertainty.

890
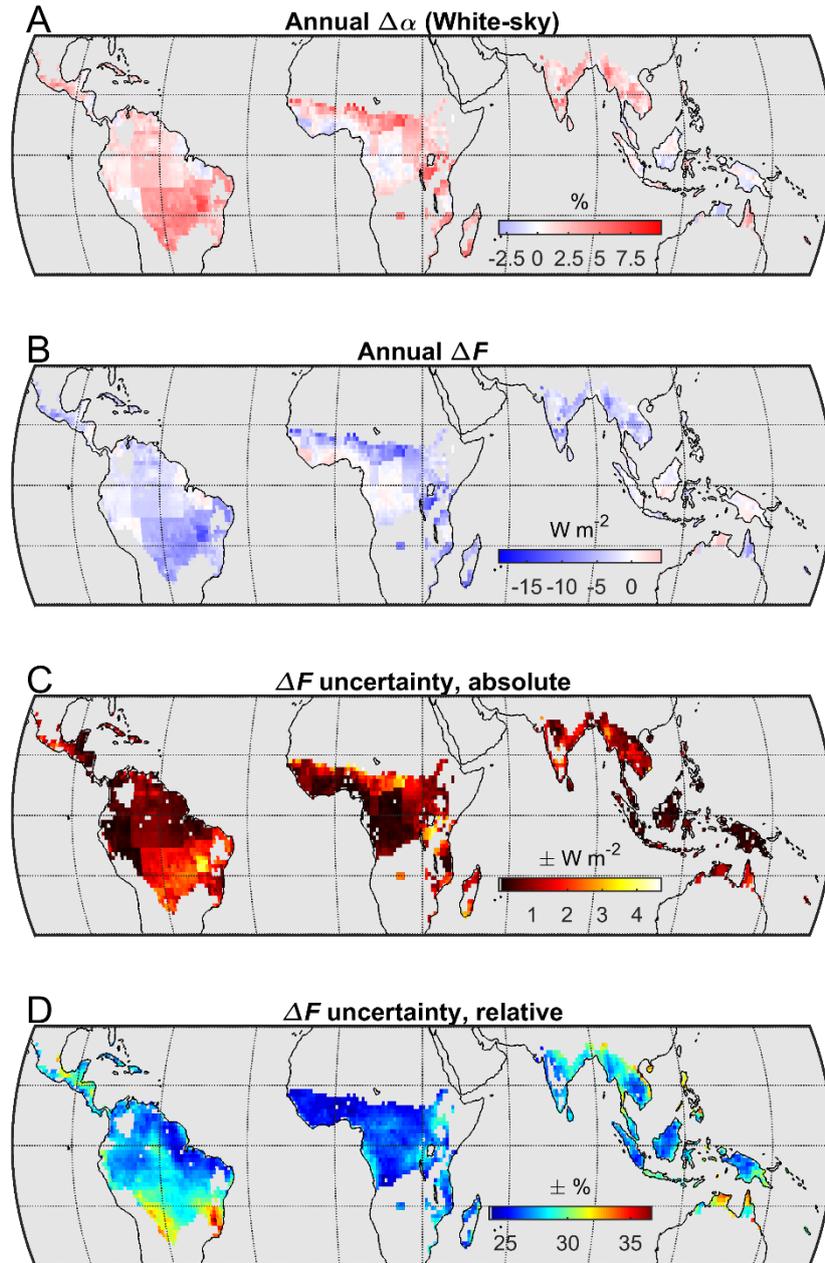
Figure 6. Example application of a CACK based on the 2001-2016 monthly mean CERES

EBAF v4 climatology to estimate the local annual mean ΔF from a hypothetical land cover

change within a CERES grid cell. A) Annual mean of the climatological (i.e., 2001-2011)

monthly mean difference in white-sky surface albedo between *croplands* and *evergreen*

broadleaved forests ($\Delta\alpha_s$) based on the 1° product of Gao *et al*. (2014); B) Annual mean

local (i.e., within grid cell) instantaneous radiative forcing (ΔF) of monthly mean $\Delta\alpha_s$

estimated with CACK; C) Absolute uncertainty (annual mean) of the CACK-based ΔF

898   estimate, including the uncertainty of $\Delta\alpha_s$; D) Relative uncertainty (annual mean) of the

899   CACK-based ΔF estimate.
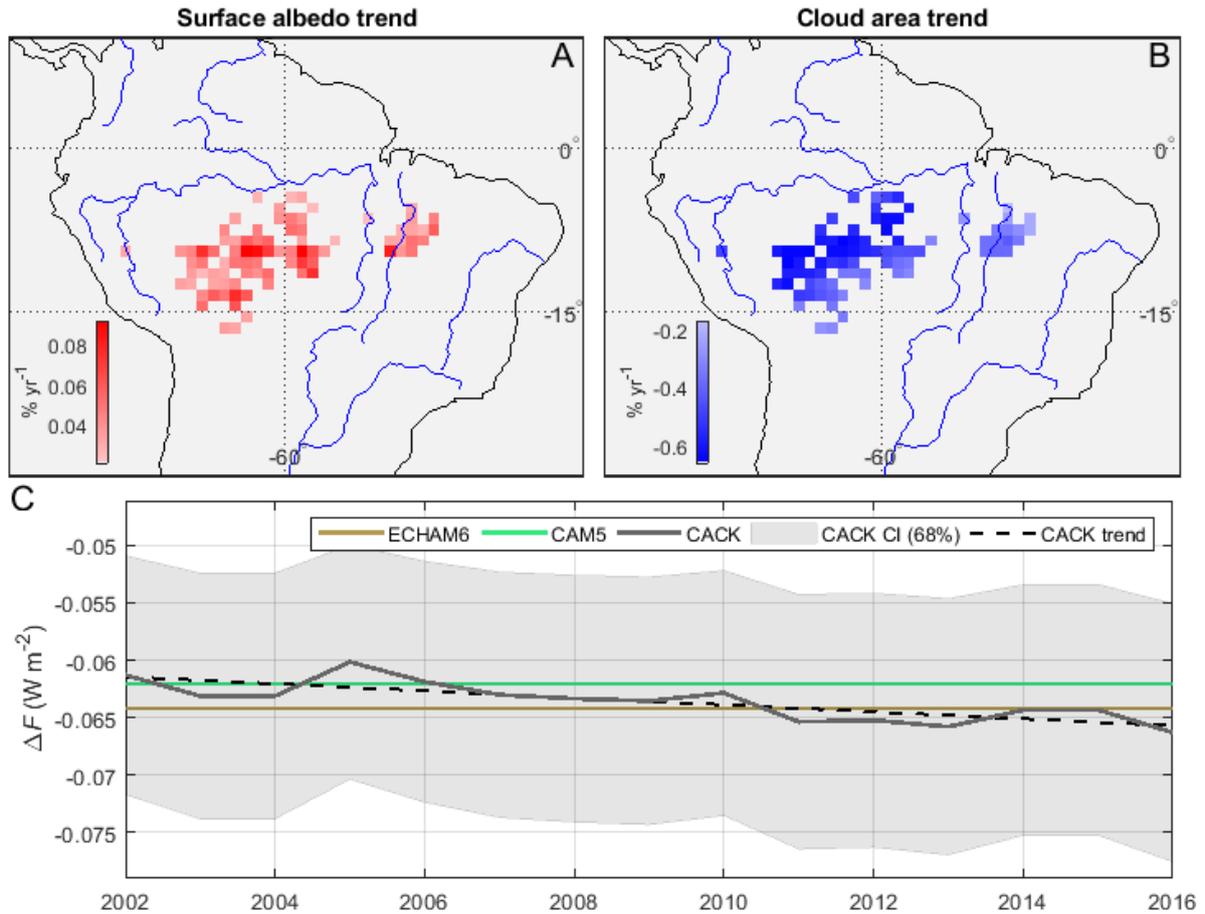
Figure 7. Example application of a temporally-explicit CACK. A) 2001-2016 statistically significant positive trends in all-sky *surface albedo* derived from CERES EBAF-Surface v4; B) 2001-2016 statistically significant negative trends in *cloud area* derived from CERES EBAF-TOA v4; C) Mean ΔF from $\Delta \alpha_s$ when estimated with the CACK, ECHAM6, and CAM5 surface albedo change kernels. ΔF is the mean of all grid cells plotted in panel A). The 1σ confidence interval ("CI") shown for CACK excludes the uncertainty component related to *physical variability*.